Journal of the Korean Astronomical Society
52: 89 ∼ 97, 2019 August

https://doi.org/10.5303/JKAS.2019.52.4.89
pISSN: 1225-4614 · eISSN: 2288-890X
http://jkas.kas.org

Merging and Fragmentation in the Solar Active Region 10930 Caused by an Emerging Magnetic Flux Tube with Asymmetric Field-Line Twist Distribution along Its Axis

Tetsuya Magara[1,2]

[1]Department of Astronomy and Space Science, Kyung Hee University, 1732 Deogyeong-daero, Giheung-gu, Yongin, Gyeonggi 17104, Korea; magara@khu.ac.kr
[2]School of Space Research, Kyung Hee University, 1732 Deogyeong-daero, Giheung-gu, Yongin, Gyeonggi 17104, Korea

Received February 28, 2019; accepted June 10, 2019

Abstract: We demonstrate the subsurface origin of the observed evolution of the solar active region 10930 (AR10930) associated with merging and breakup of magnetic polarity regions at the solar surface. We performed a magnetohydrodynamic simulation of an emerging magnetic flux tube whose field-line twist is asymmetrically distributed along its axis, which is a key to merging and fragmentation in this active region. While emerging into the surface, the flux tube is subjected to partial splitting of its weakly twisted portion, forming separate polarity regions at the solar surface. As emergence proceeds, these separate polarity regions start to merge and then break up, while in the corona sigmoidal structures form and a solar eruption occurs. We discuss what physical processes could be involved in the characteristic evolution of an active region magnetic field that leads to the formation of a sunspot surrounded by satellite polarity regions.

Key words: Sun: activity — Sun: magnetic fields — magnetohydrodynamics — methods: numerical

1. Introduction

Solar active regions are formed on the Sun when intense subsurface magnetic flux emerges into the solar atmosphere due to magnetic buoyancy (Parker 1955), which is termed flux emergence. Once formed, an active region continuously evolves as flux emergence proceeds, producing various kinds of activity such as flares and eruption. What activity is produced depends on the magnetic field configuration that arises in an active region (Low 1996; Priest & Forbes 2002; Shibata & Magara 2011). The physical properties of subsurface magnetic fields could play a role in determining configurations of active region magnetic fields. It is however difficult to detect these properties using electromagnetic waves because the solar surface behaves as an impermeable boundary towards radiative flux. On the other hand, theoretical studies provide key information on the pre-emerged state of an active region magnetic field; that is, it has the shape of a thin flux tube composed of twisted field lines (Spruit 1981; Dorch & Nordlund 1998; Abbett et al. 2000; Fan 2009).

An interesting question here is how subsurface magnetic field and the associated subsurface dynamical processes cause observed evolution of an active region; more specifically, what kind of twisted flux tube dynamically forms an active region with merging and/or fragmentation of a surface magnetic field. AR10930 is one such active region ($\beta\gamma\delta$-Mount Wilson classification; Dki-Mcintosh classification) with prominent flaring and eruptive activity (Bharti et al. 2007; Isobe et al. 2007; Yan et al. 2007; Zhang et al. 2007; Kubo et al. 2007; Su et al. 2007; Moon et al. 2007; Magara & Tsuneta 2008; Wang et al. 2008; Guo et al. 2008; Schrijver et al. 2008; Abramenko et al. 2008; Wang et al. 2008; Liu et al. 2008; Williams et al. 2009; Tan et al. 2009; Magara 2009; Harra et al. 2009; Inoue et al. 2012; Fan 2016). Figure 1 shows a time series of G-band images and corresponding soft X-ray images of AR10930 obtained by Hinode/SOT and XRT (Kosugi et al. 2007; Tsuneta et al. 2008; Golub et al. 2007), along with a schematic illustration of how the surface magnetic field evolved in this active region. The observed evolution of AR10930 may be divided into five phases: Two relatively small positive polarity regions PR1 and PR2 were distributed near a sunspot SP with negative polarity (Phase I). Then PR1 and PR2 merged together (Phase II) and a merged polarity region PR3 developed (Phase III). In this phase a prominent counterclockwise rotational flow was observed around PR3 and several arc-shaped loops were observed in soft X-ray. After that, PR3 started to break up, while inverse S-shaped sigmoidal structures were observed in soft X-ray (Phase IV). Finally a solar eruption occurred, which was accompanied by an X-class flare (Phase V).

When we investigate a twisted flux tube that causes the observed evolution of AR10930, there are suggestions from theoretical results. Merging of the same polarity regions may be caused by a partially split flux tube (Zwaan 1985; Magara 2008), and partial splitting of a flux tube is related to the degree of local field-line twist in the flux tube. Field-line twist contributes to maintaining the integrity of the flux tube as it rises

Corresponding author: T. Magara

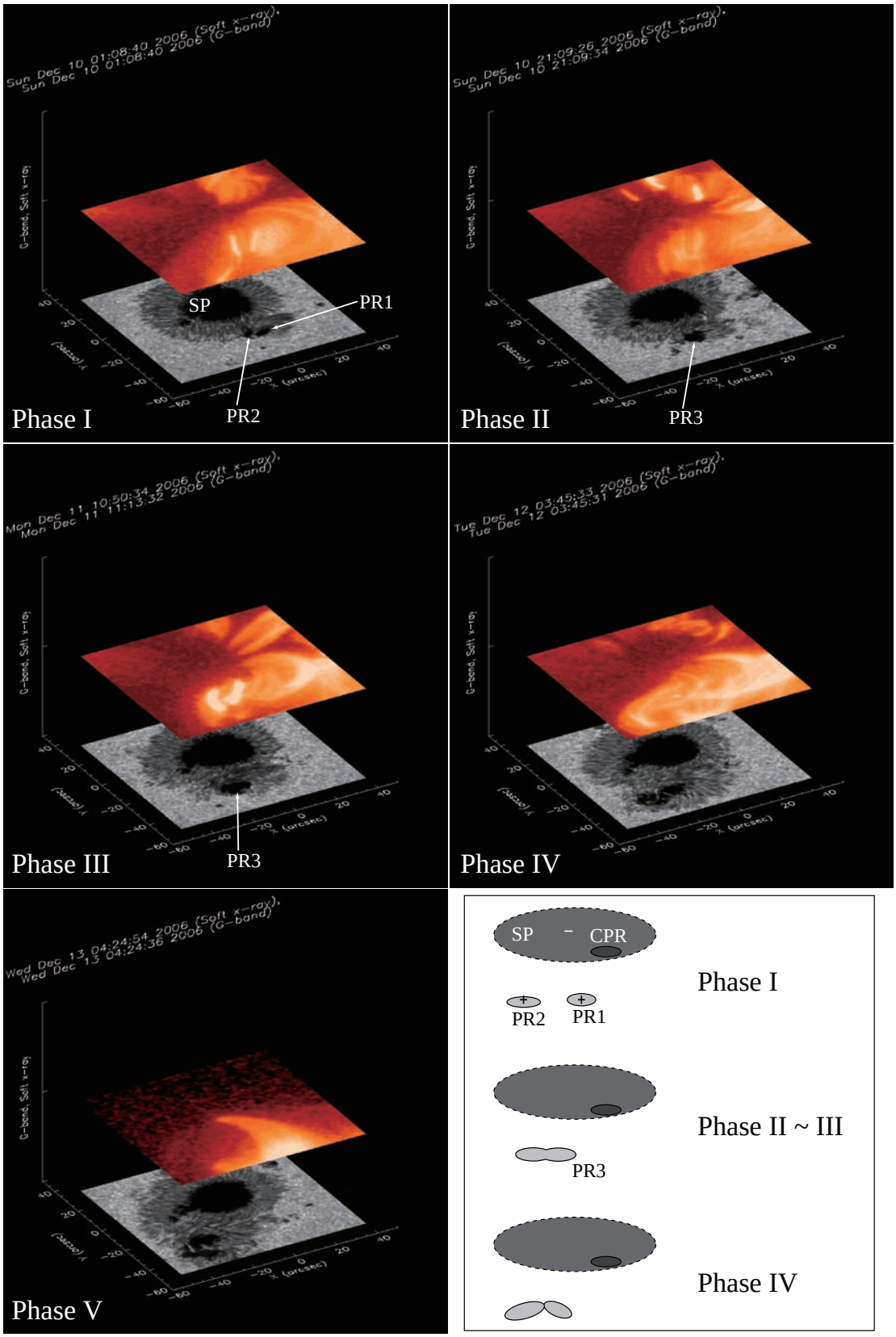

Figure 1. Time series of G-band images and corresponding soft X-ray images of AR10930 obtained by Hinode/SOT and XRT are presented at top-left (Phase I), top-right (Phase II), middle-left (Phase III), middle-right (Phase IV), bottom-left (Phase V) panels. An X-class flare occurred between Phase IV and V, at 02:40:39 UT on December 13, 2006. Evolution of magnetic polarity regions at the solar surface is schematically illustrated at the bottom-right panel.

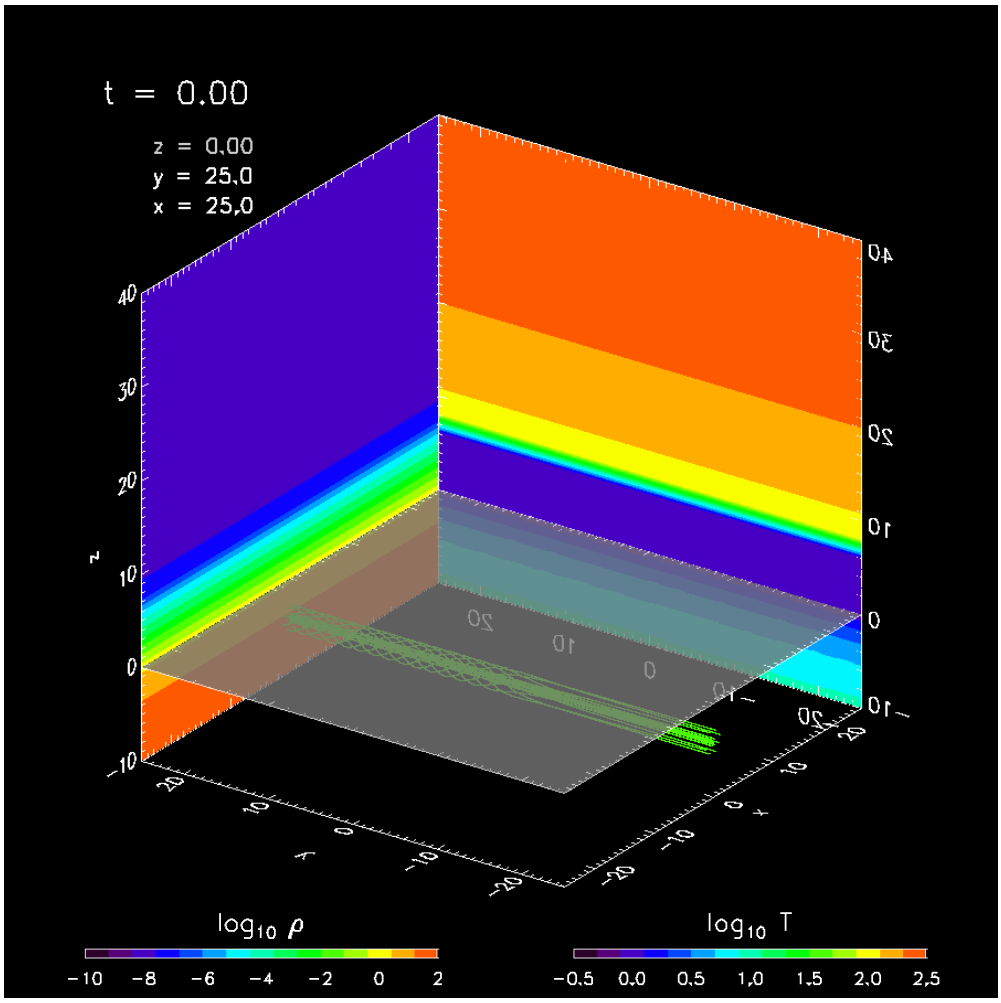

Figure 2. Initial state of the simulation. Field lines composing a flux tube are drawn in green while the color maps placed at $x = 25$ and $y = 25$ show the distributions of temperature and gas density, respectively. The translucent horizontal layer represents the solar surface.

through a subsurface region (Schüssler 1979; Longcope et al. 1996; Emonet & Moreno-Insertis 1998), so a weakly twisted portion of an emerging flux tube easily breaks up, while a strongly twisted portion forms an irrefrangible, confined polarity region such as a region CPR inside the sunspot SP in Figure 1. These results suggest that merging and fragmentation in AR10930 could be caused by an emerging flux tube whose field-line twist is strong at one emerged footpoint and weak at the other; that is, field-line twist is asymmetrically distributed along flux-tube axis.

The aim of this study is not to reproduce realistic evolution of AR10930 but to demonstrate the subsurface origin of its observed evolution. This is important for a comprehensive understanding of observed properties of the active region, because subsurface magnetic flux and subsurface dynamical processes are seamlessly connected to surface magnetic flux and surface dynamical processes, respectively. In other words, the solar surface does not behave as an impermeable boundary towards magnetic flux and dynamical processes.

In the following sections, we describe a magneto-hydrodynamic (MHD) model of merging and fragmentation in AR10930. We then discuss what physical processes could be involved in the characteristic evolution of an active region magnetic field that leads to the formation of a sunspot surrounded by satellite polarity regions.

2. MODEL DESCRIPTION

We performed an MHD simulation in the Cartesian coordinates (x, y, z) where the z-axis determines the vertical direction while the x- and y-axes form the $z = 0$ plane corresponding to the solar surface (photosphere). A simulation domain $(-200, -200, -20) \leq (x, y, z) \leq (200, 200, 180)$ is discretized into grid cells whose size is $(\Delta x, \Delta y, \Delta z) = (0.2, 0.2, 0.2)$ for $(-20, -20, -20) \leq (x, y, z) \leq (20, 20, 20)$ and it gradually increases to $(2, 2, 2)$ as $|x|, |y|$, and z increase. The total number of grid cells is $N_x \times N_y \times N_z = 379 \times 379 \times 286$.

Normalization units were $2H_p = 540$ km (length), $c_{sp} = 11$ km/s (velocity), $t_p \equiv 2H_p/c_{sp} = 49$ s (time), $\rho_p = 2.7 \times 10^{-7}$ g/cm^3 (gas density), $\rho_p c_{sp}^2 = 3.3 \times 10^5$ dyn/cm^2 (gas pressure), $T_p = 5100$ K (temperature),

and $(\rho_p c_{sp}^2)^{1/2} = 570$ G (magnetic field), where H_p, c_{sp}, ρ_p, and T_p represent the pressure scale height, adiabatic sound speed, gas density, and temperature at the photosphere.

The simulation domain is initially filled with a hydrostatic atmosphere determined by a prescribed temperature profile $T_0(z)$ and the solar surface gravity $g_\odot$, extending from a subsurface region ($z < 0$) to the corona ($z > 10$) (An & Magara 2013). In the atmosphere we place a cylindrical magnetic flux tube with a radius of $r_f = 2$ horizontally along y direction, putting its axis at $(x, z) = (0, -4)$ so that the flux tube is fully submerged in the subsurface region. The magnetic field of the flux tube has a modified Gold-Hoyle profile (Gold & Hoyle 1960), which is expressed using local cylindrical coordinates (r, θ, y) as follows:

$$B_y = B_0 \frac{1}{1 + {b_y}^2\, r^2}, \tag{1}$$

and

$$B_\theta = -B_0 \frac{b_\theta\, r}{1 + {b_\theta}^2\, r^2}, \tag{2}$$

where $\hat{y}$ and $\hat{\theta}$ determine the axial and azimuthal directions of the flux tube with left-handed field-line twist. Here $r \le r_f$ indicates radial distance from flux-tube axis and $B_0 = 11$ magnetic field strength at the axis. b_y and b_θ represent field-line twist, which are obtained by modifying a Gold-Hoyle profile; that is, $b_y = b_{max}$ (constant) and b_θ varies along the axial direction, given by the following function of y:

$$b_\theta(y) = \frac{b_{max} - b_{min}}{2} \tanh\left(\frac{y - y_c}{w}\right) + \frac{b_{max} + b_{min}}{2}, \tag{3}$$

where $b_{max} = 0.5$, $b_{min} = 0.01$, $y_c = 0$, $w = 4$. Figure 2 shows the initial state of the simulation.

The simulation starts with a rising motion applied to the initial location of the flux tube during $0 < t < t_r$, given by

$$v_z = \begin{cases} v_0 \cos\left(2\pi \frac{y}{\lambda}\right) \sin\left(\frac{\pi}{2}\frac{t}{t_r}\right) \text{ for } |y| \le \frac{\lambda}{2} \\ v_0 \cos\left(2\pi \frac{y - \left[2L - \frac{\lambda}{2}\right]\frac{|y|}{y}}{4L - 2\lambda}\right) \sin\left(\frac{\pi}{2}\frac{t}{t_r}\right) \text{ for } |y| \ge \frac{\lambda}{2} \end{cases} \tag{4}$$

where $t_r = 1$, $\lambda = 30$, $L = 200$, $v_0 = 0.25$. This motion produces an Ω-shaped emerging flux tube. We also add random perturbation for gas pressure to a subsurface domain of $-18 < z < 0$ (perturbation amplitude of gas pressure is less than 1% of its unperturbed value), which drives a convective motion in the subsurface region where a superadiabatic temperature gradient is initially applied to make this region convectively unstable (Magara 2001).

Physical quantities ρ (gas density), $\mathbf{v}$ (flow velocity), P (gas pressure), T (temperature), $\mathbf{B}$ (magnetic field), and $\mathbf{E}$ (electric field) are temporally updated by solving MHD equations given below:

$$\frac{\partial \rho}{\partial t} + \nabla \cdot (\rho\, \mathbf{v}) = 0, \tag{5}$$

$$\rho\left(\frac{\partial \mathbf{v}}{\partial t} + \mathbf{v} \cdot \nabla \mathbf{v}\right) = \frac{1}{4\pi}(\nabla \times \mathbf{B}) \times \mathbf{B} - \nabla \cdot (P\mathbf{I} - \mathbf{\Pi}) + \rho \mathbf{g}, \tag{6}$$

$$\frac{\partial P}{\partial t} + \nabla \cdot (P\, \mathbf{v}) = (\gamma - 1)\left(-P\, \nabla \cdot \mathbf{v} + \mathsf{H}_{vis} - \mathsf{L}_{rad}\right), \tag{7}$$

$$P = \frac{\rho\, \Re\, T}{\mu}, \tag{8}$$

$$\nabla \cdot \mathbf{B} = 0, \tag{9}$$

$$\frac{\partial \mathbf{B}}{\partial t} = -\, c\, \nabla \times \mathbf{E}, \tag{10}$$

$$\mathbf{E} = -\, \frac{\mathbf{v}}{c} \times \mathbf{B}, \tag{11}$$

with

$$\mu = 0.6, \quad \mathbf{g} = -g_\odot \hat{z}, \qquad \mathsf{L}_{rad} \equiv \rho\, c_V\, \frac{T - T_0(z)}{\tau_r} e^{-\left(\frac{z - z_r}{\Delta_r}\right)^2}, \tag{12}$$

where μ, $\Re$, $\mathbf{\Pi}$, H_{vis}, c_V, c, and τ_r represent the mean molecular weight, gas constant, viscous stress tensor, viscous dissipation rate, specific heat at constant volume, speed of light, and radiative relaxation time, respectively. To solve these equations, we use a modified Lax-Wendroff scheme developed for investigating viscous and resistive processes in stratified magnetized atmospheres (Magara 2015). The Reynolds number is of the order of 10^5 in the corona, where length scale is given by the typical width of a coronal loop $w \sim 5000$ km (Aschwanden 2005), while velocity scale is given by the free-fall velocity $v_f \equiv (2 g_\odot h)^{1/2} \sim 100$ km/s with $h = 20\,000$ km being assumed as the typical height of a coronal loop. A low atmospheric region is subjected to the Newton's cooling law represented by L_{rad} with $\tau_r \sim 1$ s (Stix 1991), $z_r \sim 1000$ km, $\Delta_r \sim 400$ km. This keeps the temperature around the solar surface roughly constant throughout the simulation.

Periodic boundary conditions are applied at $y = \pm 200$, and open boundary conditions at $x = \pm 200$ and $z = 180$. A fixed, impermeable boundary is placed at $z = -20$. Wave damping zones are placed near all the boundaries in order to reduce the reflection of waves at these boundaries.

3. RESULTS

3.1. Surface Evolution

Figure 3 presents a time-series of snapshots at $t = 0$ (3a), 13.2 (3b), 27 (3c), 37 (3d), 42 (3e), 50 (3f), showing the evolution of the twisted flux tube emerging into the solar surface. In each snapshot, the horizontal map at $z = 0$ shows the distribution of surface magnetic

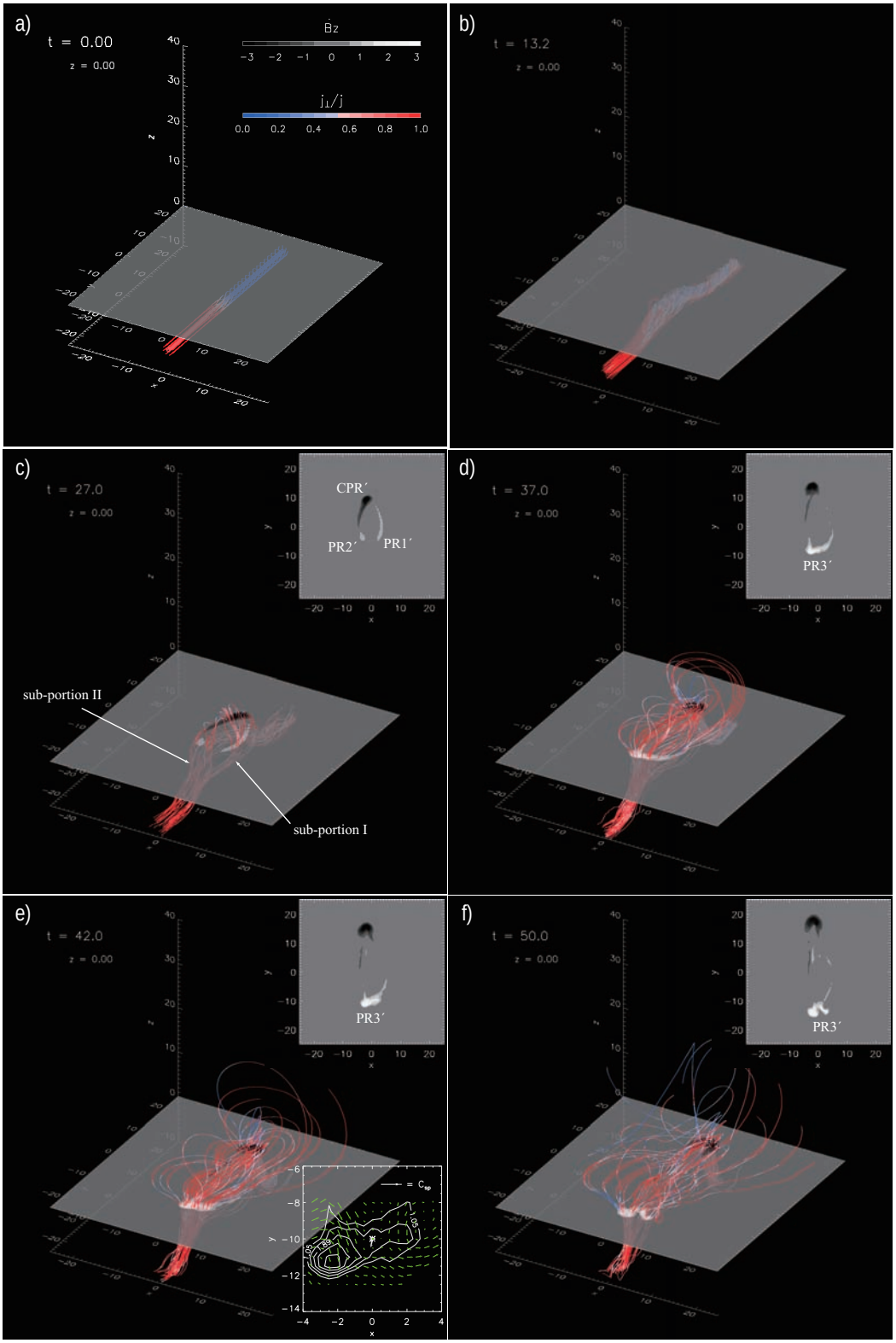

Figure 3. Time series of snapshots of the simulation taken at six different times are presented at top-left ($t = 0$), top-right ($t = 13.2$), middle-left ($t = 27$, corresponding to Phase I in Figure 1, the same hereafter), middle-right ($t = 37$, Phase II), bottom-left ($t = 42$, Phase III), bottom-right ($t = 50$, Phase IV) panels. In each panel the gray-scale map shows the distribution of surface magnetic flux, while the colors of field lines indicate the ratio of cross-field current density to total current density. A top view of surface magnetic flux maps is put at the top-right corner of panels **c**–**f**. A horizontal flow velocity field around PR3′, together with contours of surface magnetic flux, is displayed at the bottom-right corner of panel **e**, where the velocity at a selected point indicated by the asterisk and relative velocity field against it are represented by the white arrow and green arrows, respectively. Movies are provided.

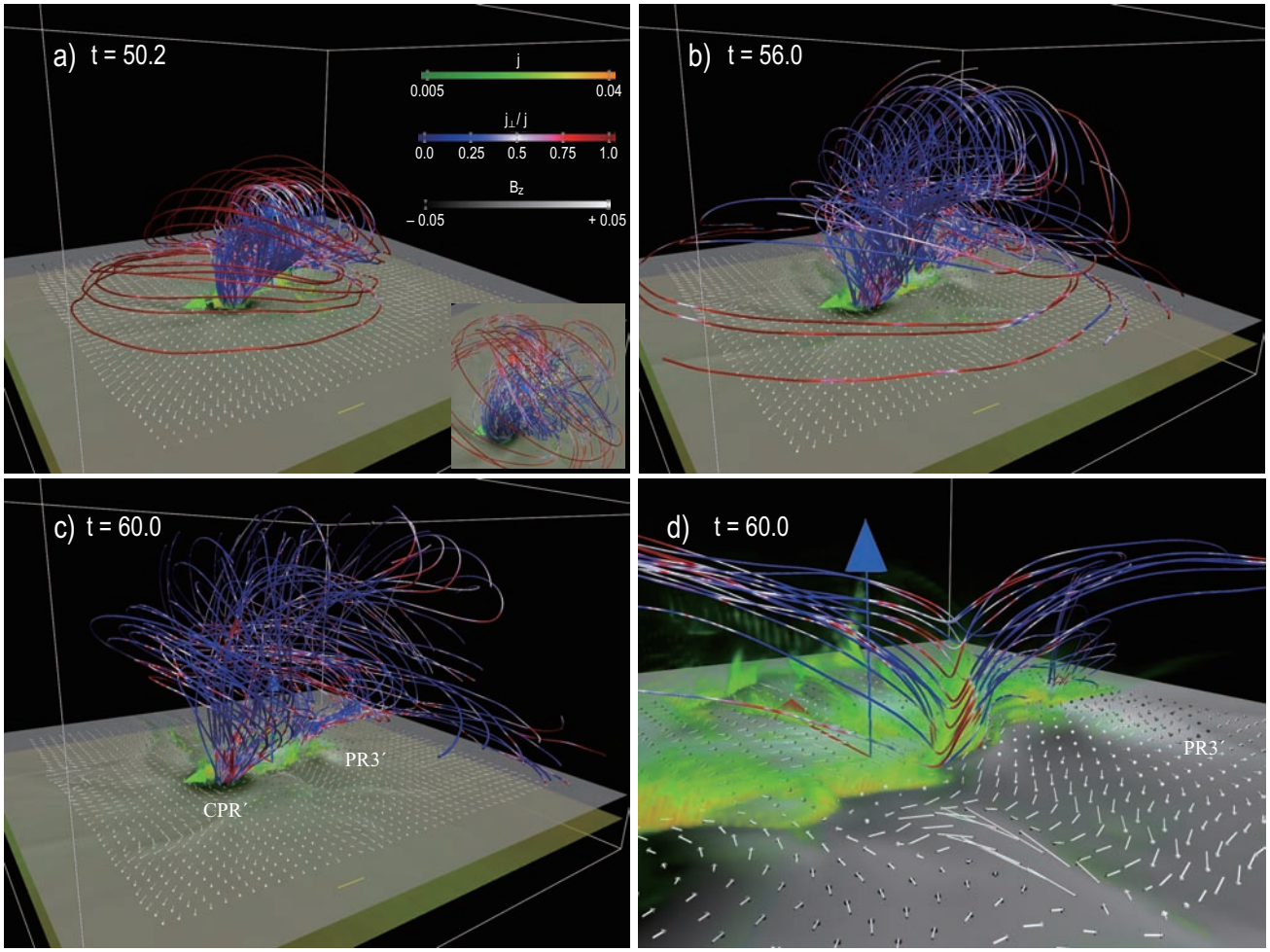

Figure 4. Time series of snapshots of the simulation taken at three different times are presented at top-left ($t = 50.2$), top-right ($t = 56$), bottom-left ($t = 60$) panels. In each panel the yellow layer represents the solar surface and the gray-scale map with a flow velocity field on it shows the distribution of magnetic flux at $z = 8$, while the colors of field lines indicate the ratio of cross-field current density to total current density and volume-rendering colors show the strength of total current density. The displayed box size is $(-80, -80, -10) \leq (x, y, z) \leq (80, 80, 90)$ and the unit of flow velocity indicated by the yellow arrows is 10 c_{sp}. A top-view snapshot at $t = 50.2$ is put at the bottom-right corner of panel **a**. A close-up snapshot of the region below erupting flux rope at $t = 60$ is presented in panel **d**. A movie is provided.

flux, while the colors of magnetic field lines indicate how much the electric current density $\mathbf{j} \equiv \nabla \times \mathbf{B}$ is locally aligned with the magnetic field; that is, when the current density is aligned with (perpendicular to) the magnetic field, a field line is locally colored blue (red). A top view of the surface magnetic flux maps is presented at the top-right corner of Figures 3c–e. The velocity field of the horizontal flow around the polarity region PR3′ is displayed at the bottom-right corner of Figure 3e.

At $t = 0$, the flux tube has a bluish portion ($y > 0$) of strong field-line twist ($b_\theta \sim b_{max}$) and a reddish portion ($y < 0$) of weak field-line twist ($b_\theta \sim b_{min}$), the former of which is close to a force-free state with the Gold-Hoyle profile $b_\theta = b_y = b_{max}$, while the latter significantly deviates from that state because b_θ is reduced from b_{max}. Since the flux tube is surrounded by a high-beta subsurface plasma, the expansion of the reddish portion due to the decrease of field-line twist is less dynamic before it emerges into the solar surface (Figure 3b).

During the early phase of emergence (Figure 3c), emerging field lines tend to assume reddish color, indicating that they experience dynamic expansion via the Lorentz force arising from the electric current crossing the magnetic field (cross-field current). The strongly twisted portion forms a confined polarity region CPR′ containing intense surface magnetic flux, while the weakly twisted portion forms separate polarity regions PR1′ and PR2′. When we look at the subsurface region, partial splitting of the weakly twisted portion proceeds during this phase, dividing it into sub-portions I and II. PR1′ is formed by the sub-portion I containing the envelop magnetic flux of the flux tube, while PR2′ is formed by the sub-portion II containing the central magnetic flux of the flux tube.

During an intermediate phase of emergence (Figure 3d), PR1′ and PR2′ start to merge together and a

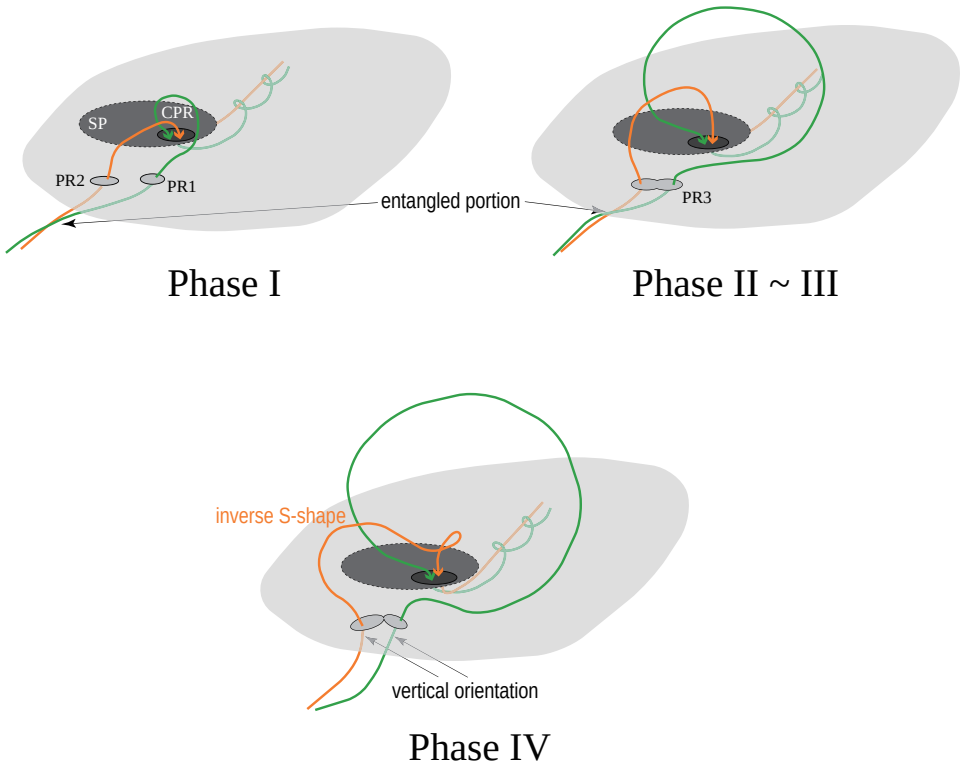

Figure 5. A comprehensive schematic illustration of observed evolution of AR10930 is presented, where subsurface information is added to the illustration presented in Figure 1. The gray translucent layers represent the solar surface, while the green and orange field lines represent the envelop and central magnetic flux of twisted flux tube, respectively.

merged polarity region PR3′ continuously develops as emergence proceeds, generating a counterclockwise rotational flow around PR3′ (Figure 3e). Figure 3e corresponds to Phase III in Figure 1, during which emerging field lines expand widely to form arc-shaped loops in the corona.

At a late phase of emergence (Figure 3f), the merged polarity region PR3′ starts to break up. This phase corresponds to Phase IV in Figure 1 (two movies are provided: `http://163.180.179.74/~magara/Download/EmergingFluxTube.mp4` for the emergence of a twisted flux tube, and `http://163.180.179.74/~magara/Download/PhotosphericFlow.mp4` for the evolution of photospheric flows).

3.2. Coronal Evolution

Next, let us focus on coronal evolution of emerging field lines at the succeeding phase during which a solar eruption occurs. Figure 4 presents a time-series of snapshots at $t = 50.2$ (4a), 56 (4b), 60 (4c and 4d), showing the evolution of emerging field lines in the corona. A top-view snapshot at $t = 50.2$ is presented at the bottom-right corner of Figure 4a, while Figure 4d shows a close-up snapshot at $t = 60$. In each panel, the yellow layer represents the solar surface and the gray-scale map and arrows on it show the distributions of magnetic flux and flow velocity at the $z = 8$ plane, while the strength of current density and the ratio of cross-field current density to total current density are shown by volume rendering colors and field-line colors, respectively.

At $t = 50.2$, there forms a coronal magnetic structure comprising outer reddish field lines where cross-field current is dominant so that they rather expand via the Lorentz force, and inner bluish field lines forming a flux rope where field-aligned current is dominant. The inner field lines assume inverse S-shaped structure, as shown by the top-view snapshot in Figure 4a. The flux rope then proceeds to eruption, as shown in Figures 4b and c (movie is provided: `http://163.180.179.74/~magara/Download/CoronalEruption.mp4`). Below the erupting flux rope, V-shaped magnetic field lines with enhanced current density at their dipped portions are formed, as shown in Figure 4d. These dipped portions are colored red, indicating that a nearly anti-parallel magnetic field configuration accompanied by intense cross-field current locally arises, which is suitable for three-dimensional magnetic reconnection producing a solar flare (Magara 2017).

4. DISCUSSION

In this section we discuss the subsurface origin of the observed evolution of AR10930. Figure 5 presents a comprehensive version of the schematic illustration in Figure 1, where subsurface information is provided. During Phase I the green and orange field lines representing the envelop and central magnetic flux of a twisted flux tube, respectively, disentangle to form separate polarity regions PR1 and PR2 at the solar surface. As emergence proceeds, an entangled portion of these field lines comes close to the solar surface, making PR1 and PR2 approach together to form a merged polarity region PR3 during Phases II and III. A strong rotational flow could be one of the features observed during these phases, as suggested by another MHD simulation (Knizhnik et al.

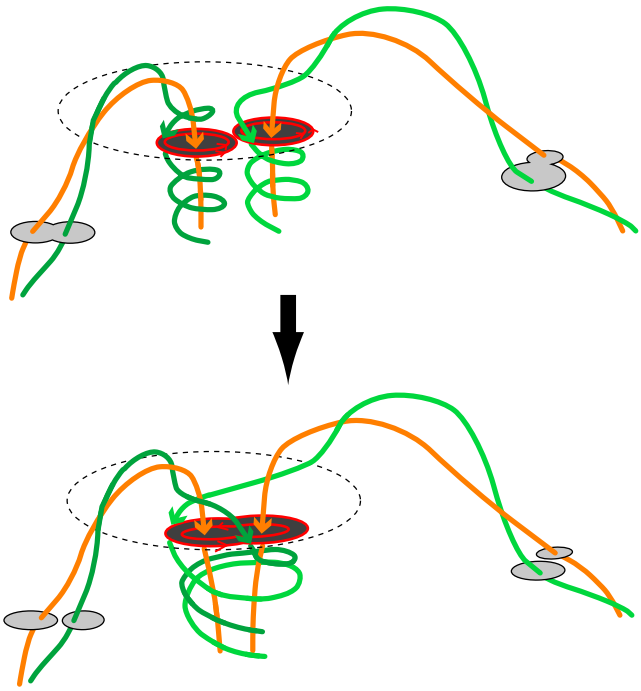

Figure 6. A scenario for the formation of a sunspot (large confined region with intense toroidal flux) surrounded by satellite polarity regions (small confined regions with intense toroidal flux) is presented. Two flux tubes whose field-line twist is asymmetrically distributed along their axes are represented by green helical field lines and orange less helical field lines. The strongly twisted portions of these flux tubes form neighboring polarity regions in a pre-sunspot area surrounded by the dashed circles, where merging of these polarity regions proceeds due to the coalescent effect of the poloidal flux represented by the red closed curves. Vector magnetic field observations made at multiple atmospheric layers may provide information on the location of active coalescence.

2018). When flux emergence enters Phase IV, emerging field lines tend to be vertical at their photospheric footpoints (see also Figure 3f), and photospheric flows easily break up the merged region PR3 composed of weakly twisted field lines. Inverse S-shaped sigmoidal structures form in the corona during this phase, as shown by the orange field line.

A flux tube whose field-line twist is asymmetrically distributed along its axis could play a key role in forming a sunspot surrounded by satellite polarity regions. Figure 6 shows how two such flux tubes interact with each other in a pre-sunspot area surrounded by the dashed circles. The green helical field lines are distributed at outer part of these flux tubes, while the orange less helical field lines are distributed at their inner part. The strongly twisted portions of these flux tubes form neighboring polarity regions in the pre-sunspot area, where the green helical field lines provide a large amount of poloidal flux represented by the red closed curves. The poloidal flux indicate that parallel currents flow through these regions, making them attract each other and eventually merge via the so-called coalescent process (Finn & Kaw 1977; Pritchett & Wu 1979; Biskamp & Welter 1980; Hayashi 1981). As coalescence proceeds, a new large polarity region is formed, and the poloidal flux distributed near the boundary of this region protects the toroidal flux contained there from leaking as well as prepares for further merging with other neighboring polarity regions. On the other hand, the weakly twisted portions of these flux tubes do not experience such coalescence because of their less amount of poloidal flux, resulting in the formation of satellite polarity regions whose size could be less than the cross section of a single flux tube when it is disrupted by photospheric flows.

As for the formation of a sunspot, a key question is how a number of flux tubes are gathered in a confined region so as to contain intense toroidal flux. Even though these flux tubes are connected to a single mother flux tube, once it is disrupted into child flux tubes, their toroidal flux essentially produces repulsive magnetic pressure force among them. This suggests that it is difficult to form a sunspot simply by gathering weakly twisted, toroidal flux-dominant child flux tubes. An alternative scenario is that when some of child flux tubes are locally twisted to provide a large amount of poloidal flux, sunspot formation proceeds via the above-mentioned coalescent process. In this scenario the distribution of field-line twist in child flux tubes plays a crucial role in determining the size of magnetic polarity regions formed at the solar surface.

ACKNOWLEDGMENTS

The author wishes to thank two reviewers for their productive comments on the manuscript. He also thanks the Kyung Hee University for general support of this work. This work was financially supported by Core Research Program (NRF-2017R1A2B4002383, PI: T. Magara) through the National Research Foundation of Korea (NRF) funded by the Ministry of Education, Science and Technology, as well as by BK21 plus program through the NRF. Visualization in Figure 4 and two movies (`PhotosphericFlow.mp4` and `CoronalEruption.mp4`) was conducted using VAPOR (Clyne & Rast 2005; Clyne et al. 2007).

REFERENCES

Abbett, W. P., Fisher, G. H., & Fan, Y. 2000, The Three-Dimensional Evolution of Rising, Twisted Magnetic Flux Tubes in a Gravitationally Stratified Model Convection Zone, ApJ, 540, 548

Abramenko, V., Yurchyshyn, V., & Wang, H. 2008, Intermittency in the Photosphere and Corona above an Active Region, ApJ, 681, 1669

An, J. M., & Magara, T. 2013, Stability and Dynamics of a Flux Rope Formed via Flux Emergence into the Solar Atmosphere, ApJ, 773, 21

Aschwanden, M. J. 2005, Physics of the Solar Corona. An Introduction with Problems and Solutions, 2nd edn. (Chichester: Praxis Publishing Ltd.)

Bharti, L., Joshi, C., & Jaaffrey, S. N. A. 2007, Observations of Dark Lanes in Umbral Fine Structure from the

Hinode Solar Optical Telescope: Evidence for Magnetoconvection, ApJ, 669, L57
Biskamp, D., & Welter, H. 1980, Coalescence of Magnetic Islands, Phys. Rev. Lett., 44, 1069
Clyne, J., & Rast, M. 2005, A Prototype Discovery Environment for Analyzing and Visualizing Terascale Turbulent Fluid Flow Simulations, Proc. SPIE, 5669, 284
Clyne, J., Mininni, P., Norton, A., & Rast, M. 2007, Interactive Desktop Analysis of High Resolution Simulations: Application to Turbulent Plume Dynamics and Current Sheet Formation, New J. Phys., 9, 301
Dorch, S. B. F., & Nordlund, A. 1998, Numerical 3D Simulations of Buoyant Magnetic Flux Tube, A&A, 338, 329
Emonet, T., & Moreno-Insertis, F. 1998, The Physics of Twisted Magnetic Tubes Rising in a Stratified Medium: Two-Dimensional Results, ApJ, 492, 804
Fan, Y. 2009, Magnetic Fields in the Solar Convection Zone, Living Rev. Sol. Phys., 6, 4
Fan, Y. 2016, Modeling the Initiation of the 2006 December 13 Coronal Mass Ejection in AR 10930: The Structure and Dynamics of the Erupting Flux Rope, ApJ, 824, 93
Finn, J. M., & Kaw, P. K. 1977, Coalescence Instability of Magnetic Islands, Phys. Fluids, 20, 72
Gold, T., & Hoyle, F. 1960, On the Origin of Solar Flares, MNRAS, 120, 89
Golub, L., Deluca, E., Austin, G., et al. 2007, The X-Ray Telescope (XRT) for the Hinode Mission, Sol. Phys., 243, 63
Guo, Y., Ding, M. D., Wiegelmann, T., & Li, H. 2008, 3D Magnetic Field Configuration of the 2006 December 13 Flare Extrapolated with the Optimization Method, ApJ, 679, 1629
Harra, L. K., Williams, D. R., Wallace, A. J., Magara, T., Hara, H., Tsuneta, S., Sterling, A. C., & Doschek, G. A. 2009, Coronal Nonthermal Velocity Following Helicity Injection Before an X-Class Flare, ApJ, 691, L99
Hayashi, T. 1981, Numerical Simulations of Forced Coalescence of Magnetic Islands Generated by a Tearing Mode Instability, J. Phys. Soc. Japan, 50, 3124
Inoue, S., Magara, T., Watari, S., & Choe, G. S. 2012, Nonlinear Force-Free Modeling of a Three-Dimensional Sigmoid Observed on the Sun, ApJ, 747, 65
Isobe, H., et al. 2007, Flare Ribbons Observed with G-Band and FeI 6302? Filters of the Solar Optical Telescope on Board Hinode, PASJ, 59, 807
Knizhnik, K. J., Linton, M. G., & DeVore, C. R. 2018, The Role of Twist in Kinked Flux Rope Emergence and Delta-Spot Formation, ApJ, 864, 89
Kosugi, T., et al. 2007, The Hinode (Solar-B) Mission: An Overview, Sol. Phys., 243, 3
Kubo, M., et al. 2007, Hinode Observations of a Vector Magnetic Field Change Associated with a Flare on 2006 December 13, PASJ, 59, 607
Liu, Y., et al. 2008, A Comprehensive View of the 2006 December 13 CME: From the Sun to Interplanetary Space, ApJ, 689, 563
Longcope, D. W., Fisher, G. H., & Arendt, S. 1996, The Evolution and Fragmentation of Rising Magnetic Flux Tube, ApJ, 464, 999
Low, B. C. 1996, Solar Activity and the Corona, Sol. Phys., 167, 217
Magara, T. 2001, Dynamics of Emerging Flux Tubes in the Sun, ApJ, 549, 608
Magara, T., & Tsuneta, S. 2008, Hinode's Observational Result on the Saturation of Magnetic Helicity Injected into the Solar Atmosphere and Its Relation to the Occurrence of a Solar Flare, PASJ, 60, 1181
Magara, T. 2008, Emergence of a Partially Split Flux Tube into the Solar Atmosphere, PASJ, 60, 809
Magara, T. 2009, Characteristic Development of Magnetic Shear in a Flare-Producing Sunspot Obtained from Vector Magnetic Field Measurements by Hinode, ApJ, 702, 386
Magara, T. 2015, MHD Simulation for Investigating the Evolutionary Path of a Solar Magnetic Field That Emerges, Structures Itself, Erupts, and Produces a Flare, PASJ, 67, L6
Magara, T. 2017, Structural Properties of the Solar Flare-Producing Coronal Current System Developed in an Emerging Magnetic Flux Tube, PASJ, 69, 5
Moon, Y.-J., et al. 2007, Hinode SP Vector Magnetogram of AR10930 and Its Cross-Comparison with MDI, PASJ, 59, 62
Parker, E. N. 1955, The Formation of Sunspots from the Solar Toroidal Field, ApJ, 121, 491
Priest, E. R., & Forbes, T. G. 2002, The Magnetic Nature of Solar Flares, A&AR, 10, 313
Pritchett, P. L., & Wu, C. C. 1979, Coalescence of Magnetic Islands, Phys. Fluids, 22, 2140
Schüssler, M. 1979, Non-Linear Dynamo Theory - Finite Amplitude Magnetic Fields with Large Scale Circulation in a Compressible Stratified Medium, A&A, 71, 79
Shibata, K., & Magara, T. 2011, Solar Flares: Magnetohydrodynamic Processes, Living Rev. Sol. Phys., 8, 6
Schrijver, C. J., et al. 2008, Nonlinear Force-Free Field Modeling of a Solar Active Region around the Time of a Major Flare and Coronal Mass Ejection, ApJ, 675, 1637
Spruit, H. C. 1981, Motion of Magnetic Flux Tubes in the Solar Convection Zone and Chromosphere, A&A, 98, 155
Stix, M. 1991, The Sun. An Introduction (Berlin: Springer-Verlag), 192
Su, Y., et al. 2007, Evolution of the Sheared Magnetic Fields of Two X-Class Flares Observed by Hinode/XRT, PASJ, 59, 785
Tan, C., Chen, P. F., Abramenko, V., & Wang, H. 2009, Evolution of Optical Penumbral and Shear Flows Associated with the X3.4 Flare of 2006 December 13, ApJ, 690, 1820
Tsuneta, S., et al. 2008, The Solar Optical Telescope for the Hinode Mission: An Overview, Sol. Phys., 249, 167
Wang, H., Jing, J., Tan, C., Wiegelmann, T., & Kubo, M. 2008, Study of Magnetic Channel Structure in Active Region 10930, ApJ, 687, 658
Wang, S. J., Yan, Y. H., Liu, Y. Y., Fu, Q. J., Tan, B. L., & Zhang, Y. 2008, Solar Radio Spikes in 2.6 - 3.8 GHz during the 13 December 2006 Event, Sol. Phys., 253, 133
Williams, D. R., Harra, L. K., Brooks, D. H., Imada, S., & Hansteen, V. H. 2009, Evidence from the Extreme-Ultraviolet Imaging Spectrometer for Axial Filament Rotation before a Large Flare, PASJ, 61, 493
Yan, Y., Huang, J., Chen, B., & Sakurai, T. 2007, Diagnostics of Radio Fine Structures around 3 GHz with Hinode Data in the Impulsive Phase of an X3.4/4B Flare Event on 2006 December 13, PASJ, 59, 815
Zhang, J., Li, L., & Song, Q. 2007, Interaction between a Fast Rotating Sunspot and Ephemeral Regions as the Origin of the Major Solar Event on 2006 December 13, ApJ, 662, L35
Zwaan, C. 1985, The Emergence of Magnetic Flux, Sol. Phys., 100, 397